Large Tunability of Strain in WO_3 Single-Crystal Microresonators Controlled by Exposure to H_2 Gas

Manca, Nicola; Mattoni, Giordano; Pelassa, Marco; Venstra, Warner J.; Van Der Zant, Herre S.J.; Caviglia, Andrea D.

DOI
10.1021/acsami.9b14501

Publication date
2019

Document Version
Final published version

Published in
ACS Applied Materials and Interfaces

ACS APPLIED MATERIALS & INTERFACES

Research Article

Cite This: ACS Appl. Mater. Interfaces 2019, 11, 44438−44443

www.acsami.org

Large Tunability of Strain in WO_3 Single-Crystal Microresonators Controlled by Exposure to H_2 Gas

Nicola Manca,*[,†,‡,§,▽] Giordano Mattoni,[†,∥,▽] Marco Pelassa,[⊥] Warner J. Venstra,[†,#] Herre S. J. van der Zant,[†] and Andrea D. Caviglia[†]

[†]Kavli Institute of Nanoscience, Delft University of Technology, P.O. Box 5046, 2600 GA Delft, The Netherlands

[‡]Dipartimento di Fisica, Universitá degli Studi di Genova, via Dodecaneso 33, 16146 Genova, Italy

[§]CNR-SPIN Institute for Superconductors, Innovative Materials, and Devices, Corso Perrone 24, 16152 Genova, Italy

[∥]Department of Physics, Graduate School of Science, Kyoto University, Kyoto 606-8502, Japan

[⊥]Dipartimento Architettura e Design, Universitá degli Studi di Genova, Stradone S. Agostino 37, 16126 Genova, Italy

[#]Quantified Air BV, Rijnsburgersingel 77, 2316 XX Leiden, The Netherlands

Supporting Information

ABSTRACT: Strain engineering is one of the most effective approaches to manipulate the physical state of materials, control their electronic properties, and enable crucial functionalities. Because of their rich phase diagrams arising from competing ground states, quantum materials are an ideal playground for on-demand material control and can be used to develop emergent technologies, such as adaptive electronics or neuromorphic computing. It was recently suggested that complex oxides could bring unprecedented functionalities to the field of nanomechanics, but the possibility of precisely controlling the stress state of materials is so far lacking. Here, we demonstrate the wide and reversible manipulation of the stress state of single-crystal WO_3 by strain engineering controlled by catalytic hydrogenation. Progressive incorporation of hydrogen in freestanding ultrathin structures determines large variations of their mechanical resonance frequencies, inducing static deformation. Our results demonstrate hydrogen doping as a new paradigm to reversibly manipulate the mechanical properties of nanodevices based on materials control.

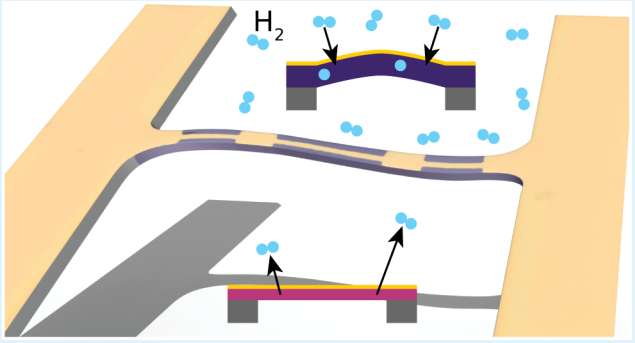

KEYWORDS: *hydrogen doping, transition metal oxides, tungsten trioxide, strain engineering, chemical strain, oxide MEMS, microelectromechanical systems*

INTRODUCTION

Complex oxides are characterized by a rich energy landscape governed by multiple thermodynamic parameters, including temperature, stress, chemical potential, and electromagnetic fields.[1−3] Phase competition in these quantum materials leads to giant responses to external stimuli associated with large and nonlinear susceptibilities. Chemical doping is a powerful control parameter to switch between their competing phases, and oxygen vacancies have often been employed to induce changes in electrical, structural, or magnetic properties, although with limited reversibility.[4−7] Hydrogen intercalation is an alternative route to effectively control the ground state of these materials, as an example, by stabilizing metallic phases and promoting lattice symmetry,[8−10] but the possibility of precisely controlling the stress state is so far lacking. A particularly interesting system with multiple competing ground states regulated by anharmonic couplings between different structural distortions is WO_3.[11] Its complex energy landscape determines large changes of its lattice and electronic properties in response to chemical doping,[12] electric fields,[13] and epitaxial strain.[14] These characteristics have important technological applications, such as electrochromic devices, smart windows,[15−17] and gas sensing where record-holding part per million (ppm) sensitivity to H_2 was recently demonstrated.[18]

Here, we show that the electromechanical response of freestanding single-crystal WO_3 microresonators can be reversibly controlled by hydrogen gas at room temperature. The incorporation of hydrogen in WO_3 thin films induces a change in the out-of-plane lattice constant up to 1.3%, an effect that we use to tune the mechanical resonances of WO_3 microbridges as their stress state changes from tensile to compressive.

Received: August 20, 2019
Accepted: October 30, 2019
Published: October 30, 2019

DOI: 10.1021/acsami.9b14501
ACS Appl. Mater. Interfaces 2019, 11, 44438−44443

RESULTS AND DISCUSSION

This experiment is performed on a 50 nm-thick single crystal WO_3 film grown on top of a Ti-terminated $SrTiO_3$ (001) substrate. The WO_3 thin film shows a flat surface with a step-and-terrace morphology that indicates good heteroepitaxial growth (film characterization in Supporting Information, Section I). A small amount of Pt, of equivalent thickness 0.2 nm, is then deposited by electron-beam evaporation to enable hydrogen intercalation, as described in the Methods section and in ref 18. We note that the hydrogen incorporation rate can be regulated by the amount of Pt catalyst: here, we choose to use a low amount of catalyst to slow down the process and monitor it as a function of time. The single-crystal character of WO_3 is confirmed by X-ray characterization, where reciprocal space maps and narrow rocking curves show that the film is coherently strained to the substrate lattice. θ–2θ scans along the (001) and (002) peaks of WO_3 present finite size oscillations, indicating high crystal quality (see Supporting Information, Section II). From the X-ray data, we extract a c axis length of 3.70 Å, in agreement with previous reports of WO_3 thin films on $SrTiO_3$.[12] Considering that in its bulk, pseudocubic phase WO_3 has a lattice constant of about 3.77 Å,[19] epitaxial lock imposed by the substrate determines an elongation of the a and b axes of about 3.4%, with a consequent decrease of the c axis that in our film amounts to −2%. The film is hence under in-plane tensile stress. This analysis indicates that the unit cell volume in thin films is slightly larger than that in bulk. This is expected and could be related to two mechanisms: a Poisson's ratio lower than 0.5 and the presence of oxygen vacancies. While the former contribution is present in the vast majority of compounds, the presence of oxygen vacancies is almost unavoidable in WO_3 thin films with optimal structural quality[12] and most probably constitutes one of the main relaxation mechanisms for epitaxial strain.

We measure the structural response of WO_3 to H_2 gas by monitoring changes in its c axis parameter by X-ray diffraction. The experimental procedure comprises the two steps illustrated in Figure 1a: The sample is initially placed at room temperature in a sealed chamber filled with 1 bar of a 20% H_2/Ar mixture for 24 h (intercalation) to achieve a stable (saturated) hydrogen doping condition. When transferred to the XRD setup, the sample is exposed to air at t = 0. In this step, hydrogen is released from the WO_3 lattice (deintercalation), and the material progressively regains its initial state. Figure 1b shows several θ–2θ scans taken during hydrogen deintercalation, where a progressive shift of the WO_3(001) peak and its finite size oscillations occurs. This shift corresponds to a change in the WO_3 c axis parameter, which is reported as a function of time in Figure 1b. In the hydrogen-doped state at t = 5 min, we measure c_{WO_3} = 3.75 Å, indicating an increase of about 1.25% with respect to the undoped condition. Upon hydrogen deintercalation, c_{WO_3} progressively decreases and recovers the value of the initial state after about 1 h. This indicates that hydrogen determines a large and reversible expansion of the WO_3 lattice, with a magnitude comparable to what has been previously reported upon the formation of oxygen vacancies or intercalation of alkali metals.[12,19,20]

The large lattice expansion induced by hydrogen doping offers the interesting possibility to control the mechanical stress of the material in a reversible manner. To explore this possibility, we realize WO_3 freestanding microbridges. The structures are fabricated by using lithographic patterning and combined dry/wet etching processes to remove the $SrTiO_3$ substrate, a procedure similar to the one used in previous reports[4] (see also Methods section and Supporting Information, Section III). Figure 2a shows the false-color micrograph of a typical WO_3 microbridge acquired by scanning electron microscopy. The freestanding structure (5 μm-wide, 110 μm-long) is composed of a 50 nm-thick WO_3 crystalline thin film (purple) and 50 nm-thick gold elements (yellow) comprising two 5 μm × 5 μm mirrors and a 1 μm-wide microwire that runs throughout the freestanding region. The mirrors are used to reflect the laser light employed to measure the mechanical motion of the bridge in an optical lever geometry (Figure 2b), while the microwire provides a low-impedance electrical channel required for the electrical excitation. By applying an alternating electrical current through the gold wire, the microstructure is mechanically actuated via the magnetomotive and electrothermal mechanisms (see Methods). The typical mechanical spectrum of a pristine 110 μm-long microbridge is shown in Figure 2c. We also fabricated microbridges of other lengths between 50 and 110 μm, all of which show similar spectra (see Supporting Information, Section IV). The fundamental resonance mode of the longer beams shows a better signal-to-noise ratio compared to the shorter ones, as expected due to a larger deflection. Furthermore, a higher quality factor is observed, which is attributed to lower clamping losses (see Supporting Information, Section V). For these reason, we focus on the 110 μm-long microbridge to investigate the changes induced by hydrogen incorporation.

The simultaneous mechanical and electrical characterization is performed in a vacuum chamber with variable gas environment, optical access, and a controlled sample temperature fixed at 25 °C. The WO_3 device is initially in an undoped condition, and we measure its mechanical spectrum as a

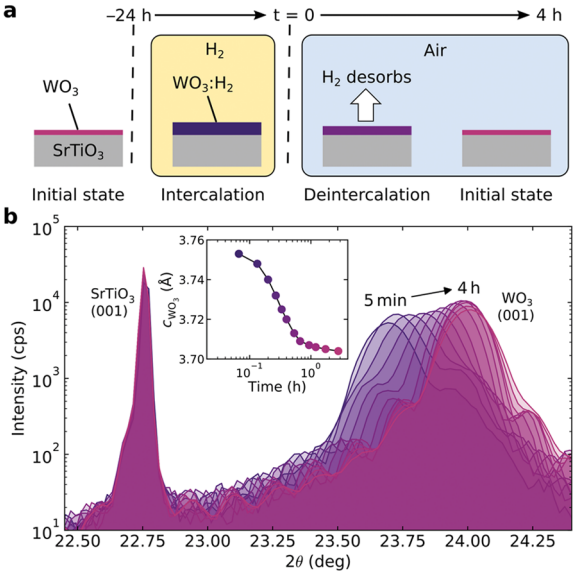

Figure 1. Lattice expansion due to hydrogen doping in WO_3 thin films. (a) Schematic representation of the experiment showing hydrogen intercalation in a 20% H_2/Ar mixture and deintercalation in air. (b) X-ray scan showing the sharp (001) peak of the $SrTiO_3$ substrate and WO_3 (001) peak with its finite size oscillations during hydrogen deintercalation. The inset shows the variation of WO_3 c axis length as a function of time.

DOI: 10.1021/acsami.9b14501
ACS Appl. Mater. Interfaces 2019, 11, 44438−44443

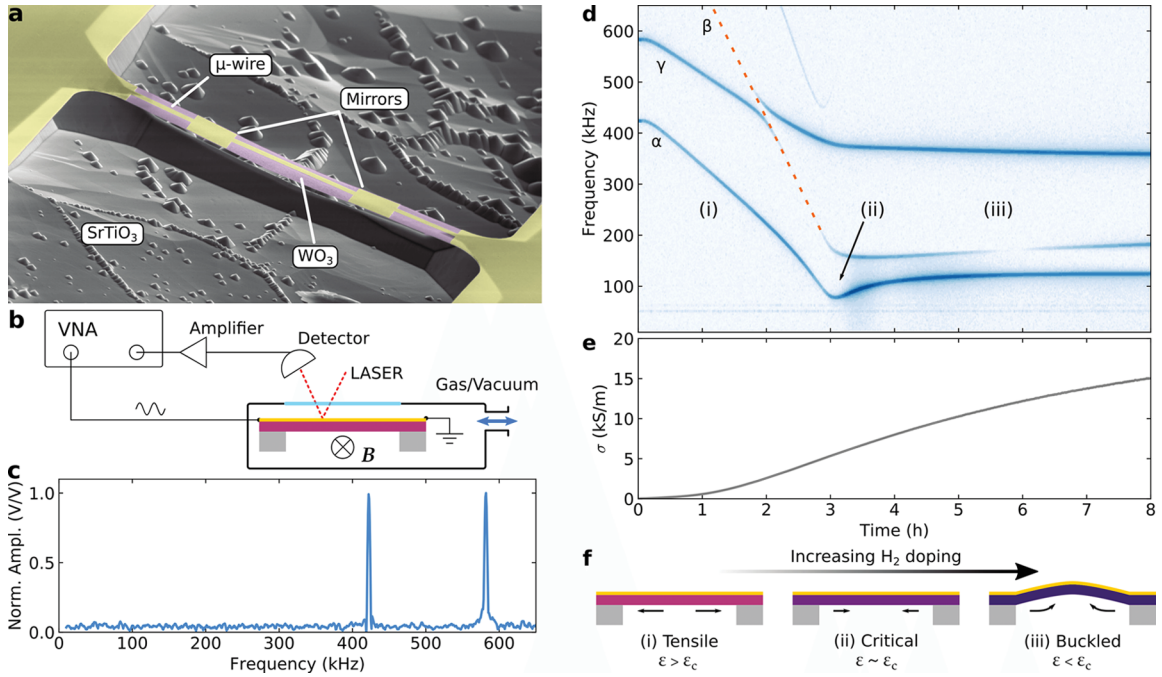

Figure 2. Hydrogen doping of single-crystal WO_3 microbridges. (a) Scanning electron micrograph in false colors of the measured device. (b) Schematic of the experimental setup (VNA, vector network analyzer). (c) Mechanical spectrum of a 110 μm-long microbridge in the pristine state. (d) Colormap of the mechanical spectra of the microbridge in (a) as a function of time when exposed to 5 mbar of 20% H_2/Ar gas mixture and (e) electrical conductivity measured at the same time. The color scale in (d) is linear and normalized in V/V. (f) Illustration of the three regimes identified in (d).

function of time in Figure 2d. Details of the optical setup employed in this experiment are reported in the Supporting Information, Section VI. At $t = 0$, we introduce a 20% H_2/Ar mixture at a low pressure (0.5 mbar) to follow the hydrogen intercalation dynamics with minimal damping of the mechanical motion. Hydrogen doping results in a dramatic change in the mechanical behavior of the microbridge, which can be divided into three distinct regions: (i) a steep decrease of the eigenfrequencies, (ii) a transitional regime, and (iii) a flat response. The lowest mechanical mode α has a smooth behavior across different regions and corresponds to the first flexural mode, as discussed in the following. At $t = 0$, the WO_3 microbridge is in a tensile strain state originating from the lattice mismatch with the $SrTiO_3$ substrate. In this condition, the structure can be schematically modeled as an ideal thin and long double-clamped beam where the flexural resonance frequencies are given by the Euler–Bernoulli equation[21]

$$f_n(\varepsilon) = a_n \frac{t}{l^2}\sqrt{\frac{E}{\rho}\left(\frac{1}{(1-\nu^2)} + b_n \varepsilon \left(\frac{l}{t}\right)^2\right)} \quad (1)$$

with resonance frequency f_n relative to the nth mode, axial strain ε, Young modulus E, density ρ, Poisson ratio ν, length l, and thickness t. a_n and b_n are numerical coefficients related to the mode shape. Equation 1 shows that the mechanical eigenfrequencies of the microbridge change as a function of strain ε. In our experiment, ε changes continuously over time due to the large WO_3 lattice expansion during hydrogen intercalation (Figure 1). The most dramatic effect is observed in region (i), where the relaxation of the initial tensile strain results in a large drop of the resonance frequencies. According to eq 1, the frequency of the first flexural mode $f_1(\varepsilon)$ is expected to reach zero at the critical strain value

$$\varepsilon_c = -\frac{1}{1-\nu^2}\left(\frac{t}{l}\right)^2 \frac{1}{b_1} \quad (2)$$

However, in real systems, this is typically not observed because device asymmetry causes the frequency to reach a smooth minimum at the finite strain value ε_c.[22] In our experiment, this occurs in region (ii) at $t \sim 3$ h, where the resonance frequency of the lowest mode α shows a minimum at $f = 80$ Hz, about one-fifth of its initial value. A further increase in the compressive strain causes out-of-plane buckling. This occurs in region (iii), where eq 1 is not applicable and the resonance frequency of α increases again as the compressive strain energy is stored in the form of out-of-plane deformation (buckling). At the onset of the buckled state, the frequencies of the odd mechanical modes are expected to rise slightly,[22−24] consistent with the small frequency increase of α in region (ii). Multiple higher-order modes are visible in the spectral map of Figure 2d, with frequencies above α. Their frequencies cannot be represented by a simple string resonator because interfacial stress and nonuniform mass distribution play an important role. These resonances are probably related to torsional and flexural modes of even order, which show different responses to strain,[23] as discussed in the last part of this work. An avoided crossing between modes β and γ occurs at around $t = 2$ h, indicating a strong coupling between the mechanical modes. This feature arises as each mode shows a different tuning slope with applied compressive stress.[23−25] Finally, we note that the data reported in Figure 2d are in good qualitative agreement with similar measurements performed during hydrogen deintercalation in air, thus showing good reversibility of the process (Supporting Information, Section VII).

During hydrogen intercalation, we also measure the time dependence of the electrical conductivity of WO_3 (σ_{WO_3}),

DOI: 10.1021/acsami.9b14501
ACS Appl. Mater. Interfaces 2019, 11, 44438−44443

which is reported in Figure 2e. In our device design, the conductivity of the whole microbridge is always determined by the gold microwire, whose constant electrical resistance (50 Ω) is much lower than that of WO_3 at any level of hydrogen doping. For this reason, we monitor σ_{WO_3} on a separate region of the film close to the microbridge. The data shows the progressive metallization of the material due to electronic doping, in agreement with previous reports.[18] Hydrogen intercalation progresses smoothly during the whole experiment, and saturation occurs only toward the end of the measured time span (t > 8 h). This indicates that between t = 4 and 8 h the amount of hydrogen in the WO_3 lattice is significantly increasing, even if the mechanical modes show a flat response. We note that, albeit the suspended WO_3 microbridge has a higher surface area exposed to H_2 gas compared to the clamped film, in both cases the Pt catalyst is present only on the top surface, thus determining the same rate of hydrogen intercalation. Furthermore, the rate of hydrogen dynamics in this experiment is significantly longer than during the XRD measurements of Figure 1 because of the low hydrogen pressure and the different rates of intercalation and deintercalation.[18] The observed evolution of the microbridge mechanical states is schematically summarized in Figure 2f.

A strong evidence of the insurgence of a buckled state upon the intercalation of hydrogen can be obtained by optical microscopy. For this purpose, we report in Figure 3 a series of

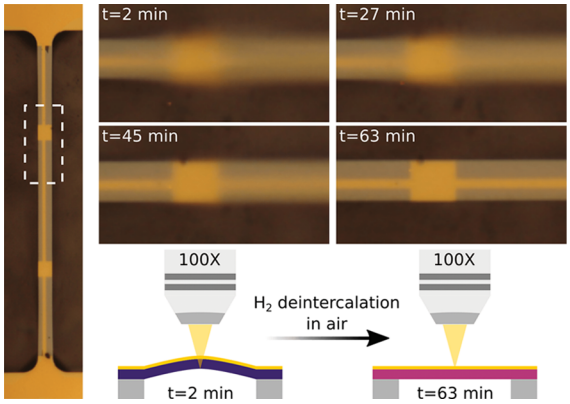

Figure 3. Relaxation of the buckled state upon hydrogen deintercalation. Optical images of the WO_3 microbridge of Figure 2a initially in a condition of saturated doping and exposed to air at t = 0. The white dashed rectangle indicates the magnified region. The schematic drawing illustrates how relaxation of the buckled state brings back the microbridge in the microscope focal plane.

photographs showing one gold mirror of the microbridge. For this experiment, the microbridge is first prepared in a saturated-doping state, and at t = 0 it is exposed to air at room temperature, the same procedure used in Figure 1. The photographs are acquired at different times with an objective lens (depth of field of about 0.7 μm) whose focal plane is fixed to have in focus the clamped edges of the microbridge. In the initial state at t = 2 min, the mirror is out of focus, indicating static deformation in the direction perpendicular to the focal plane. The structure gradually gets more in focus at t = 45 min, and at t = 63 min, after about 1 h in air, the whole microbridge is in focus, indicating the recovery of a flat state in the undoped conditions. We note that this time span of hydrogen deintercalation in 1 bar of air is comparable to the one of the XRD measurements of Figure 1 and, as previously discussed, much faster than the slow dynamics observed in Figure 2.

To better understand the changes of the WO_3 microbridge mechanical properties, we perform a finite element analysis as a function of strain (details in Methods and Supporting Information, Section VIII). We report in Figure 4a,b the strain

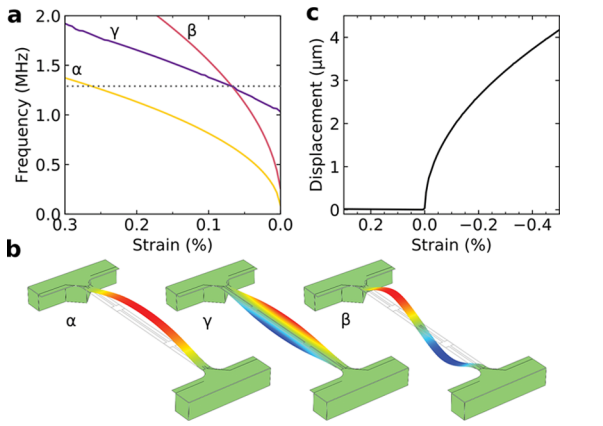

Figure 4. Finite element simulation of a strained WO_3 microbridge. (a) Strain dependence of the first flexural (α and β) and torsional (γ) mechanical modes and (b) corresponding mode shapes. (c) Vertical displacement of the microbridge center as a function of strain.

dependence of the three lowest modes of the simulated device and the corresponding mode shapes. The trend of the frequencies well represents our experimental data, with a rapid decrease of the first and second flexural modes α and β and a slower variation of the torsional mode γ. Due to their different slopes, β and γ intersect at about f = 1.3 MHz (frequency value indicated by the gray dotted line). Also, the presence of a mode crossing is consistent with our experimental results, where it occurs around f = 0.45 MHz (Figure 2d). We note that the experimental crossing frequency is about three times smaller than the simulated one, a discrepancy probably caused by the fact that we used values of E_{WO_3} and ν_{WO_3} from first principles since no experimental data is available in the literature.[26] However, the strain value corresponding to the crossing point in our simulations is weakly dependent on E and ν (Supporting Information, Section VIII) and can thus be used as a reference to estimate the in-plane strain of our experimental device. As an additional reference point, we note that in the experimental data of Figure 2d, the frequency of mode α at t = 0 corresponds approximately to the frequency of the avoided mode crossing (f = 0.45 MHz). Using this information in Figure 4a, we can estimate the initial strain of the microbridge to be about ε_0 = 0.25% (crossing of mode α with the gray dotted line). Surprisingly, this value is rather small compared to the epitaxial mismatch of 3.4% between WO_3 and the $SrTiO_3$ substrate. However, this can be explained considering that oxide compounds can easily accommodate stress with the formation of dislocations or point defects, such as oxygen vacancies. In particular, previous work shows that a low concentration of oxygen vacancies during the growth of WO_3 is sufficient to determine a relatively large lattice expansion, thus effectively relaxing the strain while maintaining a high crystal quality.[12]

It is possible to estimate the total experimental variation of the microbridge strain from the c axis expansion Δc measured by XRD (Figure 1). For this purpose, we note that by taking

DOI: 10.1021/acsami.9b14501
ACS Appl. Mater. Interfaces 2019, 11, 44438−44443

into account the different constraints for an epitaxial film and a freestanding structure we have

$$\frac{\Delta c}{c_0} = \left(\frac{1+\nu}{1-\nu}\right)\Delta\varepsilon \tag{3}$$

with out-of-plane lattice parameter in the undoped state c_0, Poisson ratio ν, and total strain variation $\Delta\varepsilon$ (see Supporting Information, Section IX). With the parameters employed in the simulation, we obtain $\Delta\varepsilon = 0.75\%$. Taking the initial microbridge strain as +0.25% for the discussion above, we can estimate the strain in the saturated doping condition to be about −0.5%. On the basis of this analysis, we calculate the vertical displacement of the microbridge center as a function of strain in Figure 4c. For positive (tensile) strain, the displacement is negligible, while beyond the critical value ε_c, the structure relaxes the negative (compressive) strain by bending. At $\varepsilon = -0.5\%$, the simulation gives a displacement of 4 μm, a value compatible with the optical measurements of Figure 3. We note that the crossing point between tensile and compressive strain ($\varepsilon_c \sim 0$) lies at one third of the estimated range of experimental strain in Figure 4c. This is in good agreement with the experimental data of Figure 2d, where the critical condition of region (ii) lies also at about one third of both the total time and the electrical conductivity spans. Finally, we emphasize that in MEMS/NEMS devices, it is particularly difficult to generate large compressive stress, a condition that usually requires additional components such as electrostatic actuators, piezoelectric elements, or resistive heaters. These components present important drawbacks such as difficulty of focusing the actuation force on the resonator beam, hurdles in high-purity material fabrication, and insurgence of high temperatures. Our approach involving chemical doping proved to be a fundamental step forward over the present difficulties, providing a pathway for strong and localized strain control of micro and nanodevices.

CONCLUSIONS

In summary, we demonstrated a new effective approach for controlling in situ the stress state of oxide-based freestanding structures. We achieved reversible control of the mechanical properties of single-crystal WO_3 microbridges, where the large lattice expansion due to hydrogen intercalation allowed us to finely tune the stress state from tensile to compressive, with a final buckled configuration. The proposed approach could be extended in two directions: by exploring the mechanical response of other oxides micromechanical systems to hydrogen doping and by realizing full-oxide heterostructures comprising a WO_3 layer acting as functional strain-tuning element. Our work highlights the potential of complex oxides to realize tunable nanomechanical systems or novel sensing devices.

METHODS

Device Fabrication. The single-crystal, 50 nm-thick WO_3 thin film on TiO_2-terminated $SrTiO_3(001)$ substrate was grown by pulsed laser deposition using 500 °C substrate temperature, 8×10^{-2} oxygen pressure, 1 J cm^{-2} laser fluence, and 1 Hz repetition rate. Pt was deposited by e-beam evaporation, and its growth rate was monitored using a quartz microbalance. The process was stopped at an equivalent thickness of 0.2 nm. The microbridge structures were realized by a two-step electron-beam patterning using PMMA resist. The first patterning step was used to define the geometry of high-reflectivity mirrors and the low-impedance microwire, followed by electron-beam evaporation of a 5/45 nm Ti/Au overlayer and lift-off in acetone. The second patterning step defined the microbridge mesa and was followed by a 6 min Ar etching process (10 mA beam current, 500 eV beam energy, and 7×10^{-4} mbar pure Ar atmosphere) during which a total of 60 nm of the $WO_3/SrTiO_3$ heterostructure was removed. The microbridges are finally made freestanding by selectively etching the $SrTiO_3$ substrate in a 4% aqueous solution of HF at 30 °C for 30 min, resulting in a total of 7 μm vertical distance between the etched substrate and the freestanding WO_3. This process has a high fabrication yield with more than 90% of the patterned microbridges freestanding and ready to be measured.

Measurement Setup. The electrical conductance measurements were performed using a four-probe DC configuration on a patterned square of the clamped WO_3 film. Contacts to the WO_3 film were provided by wire-bonding Ti/Au metal pads. The mechanical measurements were performed in a custom setup featuring a controlled gas atmosphere, temperature stability of ±50 mK, motion detection of microstructures with optical lever technique and electrical pass-through. The optical images of Figure 3 were acquired with an Olympus microscope equipped with a UMPlan FI 100×/0.90 objective lens.

Mechanical Measurements. The mechanical modes of the microbridges are excited by biasing the device with an AC voltage across the metal microwire of the form $V(t) = V_0(1 + \sin(\omega t))$. Two concurrent mechanisms determine the appearance of a mechanical force: magnetomotive and electrothermal. The magnetomotive mechanism arises from the Lorentz force exerted on the current flowing in the microbridge by the magnetic field of a permanent magnet located in the sample chamber. The electrothermal mechanism is due to the periodic thermal expansion and contraction of the microbridge determined by periodic Joule heating. Since the resistance of the metal microwire (~50 Ω) is much lower than that of the WO_3 bridge, even in its most doped state, the current flowing in the wire does not depend on WO_3 doping conditions, hence providing a constant excitation magnitude. We note that the film thickness of 50 nm was chosen to have resonance frequencies falling within the accessible measurement range of our detector (2 MHz) and homogenous doping in the out-of-plane direction. Thinner samples would improve both aspects but with the risk of lowering the fabrication yield. The data in Figure 2 were acquired using an Agilent HP4395a vector network analyzer with a 1 kHz bandwidth and 5 averages taken over a period of 20 s. Details of the optical setup are reported in the Supporting Information, Section VI.

Finite Element Simulation. Finite element analysis was performed in COMSOL Multiphysics using the structural mechanic module. The calculations employed the "static" and "prestressed eigenfrequency" solvers with a parametric sweep of the strain value. The mechanical parameters used to model the WO_3 microbridge are $E = 300$ GPa, $\nu = 0.25$, and $\rho = 7600$ kg m^{-3}, while Au was modeled using the standard material library provided by the software. Further details and device geometry are discussed in Supporting Information, Section VIII.

ASSOCIATED CONTENT

Supporting Information

The Supporting Information is available free of charge on the ACS Publications website at DOI: 10.1021/acsami.9b14501.

Growth and surface analysis of WO_3 thin film, structural analysis by X-ray diffraction, device fabrication, pictures of the final devices, mechanical properties of microbridges of different lengths, details of the finite element model, and analytic model of strain in clamped and freestanding thin films (PDF)

Supporting video shows a WO_3 microbridge over time during hydrogen deintercalation (AVI)

DOI: 10.1021/acsami.9b14501
ACS Appl. Mater. Interfaces 2019, 11, 44438−44443

AUTHOR INFORMATION

Corresponding Author

*E-mail: manca@fisica.unige.it.

ORCID

Nicola Manca: 0000-0002-7768-2500

Giordano Mattoni: 0000-0002-3678-9168

Author Contributions

[▽]N.M. and G.M. contributed equally to this work.

Author Contributions

N.M. and G.M. conceived this work, designed the experiments, and performed the mechanical measurements. N.M. designed the device geometry and performed the finite element analysis. G.M. fabricated the device and performed the XRD, SEM, and optical measurements. M.P. provided the structural analysis leading to eq 3. W.J.V. designed and realized the mechanical characterization setup. N.M. and G.M. wrote the manuscript. A.D.C. supervised the project. All authors discussed the results and contributed to the final manuscript.

Notes

The authors declare no competing financial interest.

ACKNOWLEDGMENTS

We thank P.G. Steeneken, L. Pellegrino, and D. Marré for helpful discussions and valuable comments on the manuscript. This work was supported by The Netherlands Organisation for Scientific Research (NWO/OCW) as part of the Frontiers of Nanoscience program (NanoFront). This work was supported by the EU through the European Research Council Advanced grant no. 677458 (AlterMateria). We acknowledge received funding from the project Quantox of QuantERA ERA-NET Cofund in Quantum Technologies (grant agreement no. 731473) implemented within the EU H2020 Programme.

REFERENCES

(1) MacManus-Driscoll, J. L.; Zerrer, P.; Wang, H.; Yang, H.; Yoon, J.; Fouchet, A.; Yu, R.; Blamire, M. G.; Jia, Q. Strain Control and Spontaneous Phase Ordering in Vertical Nanocomposite Heteroepitaxial Thin Films. *Nat. Mater.* **2008**, *7*, 314−320.

(2) Rondinelli, J. M.; May, S. J.; Freeland, J. W. Control of Octahedral Connectivity in Perovskite Oxide Heterostructures: An Emerging Route to Multifunctional Materials Discovery. *MRS Bull.* **2012**, *37*, 261−270.

(3) Ramesh, R.; Schlom, D. G. Creating Emergent Phenomena in Oxide Superlattices. *Nat. Rev. Mater.* **2019**, *4*, 257.

(4) Manca, N.; Pellegrino, L.; Marré, D. Reversible Oxygen Vacancies Doping in $(La_{0.7},Sr_{0.3})MnO$ Microbridges by Combined Self-Heating and Electromigration. *Appl. Phys. Lett.* **2015**, *106*, 203502.

(5) Swallow, J. G.; Kim, J. J.; Maloney, J. M.; Chen, D.; Smith, J. F.; Bishop, S. R.; Tuller, H. L.; Van Vliet, K. J. Dynamic Chemical Expansion of Thin-Film non-Stoichiometric Oxides at Extreme Temperatures. *Nat. Mater.* **2017**, *16*, 749−754.

(6) Yao, L.; Inkinen, S.; Van Dijken, S. Direct Observation of Oxygen Vacancy-Driven Structural and Resistive Phase Transitions in $La_{2/3}Sr_{1/3}MnO_3$. *Nat. Commun.* **2017**, *8*, 14544.

(7) Zhang, K. H. L.; Li, G.; Spurgeon, S. R.; Wang, L.; Yan, P.; Wang, Z.; Gu, M.; Varga, T.; Bowden, M. E.; Zhu, Z.; Wang, C.; Du, Y. Creation and Ordering of Oxygen Vacancies at $WO_{3-\delta}$ and Perovskite Interfaces. *ACS Appl. Mater. Interfaces* **2018**, *10*, 17480−17486.

(8) Kïlïç, Ç.; Zunger, A. n-Type Doping of Oxides by Hydrogen. *Appl. Phys. Lett.* **2002**, *81*, 73−75.

(9) Wei, J.; Ji, H.; Guo, W.; Nevidomskyy, A. H.; Natelson, D. Hydrogen Stabilization of Metallic Vanadium Dioxide in Single-Crystal Nanobeams. *Nat. Nanotechnol.* **2012**, *7*, 357−362.

(10) Yoon, H.; Choi, M.; Lim, T.-W.; Kwon, H.; Ihm, K.; Kim, J. K.; Choi, S.-Y.; Son, J. Reversible Phase Modulation and Hydrogen Storage in Multivalent VO_2 Epitaxial Thin Films. *Nat. Mater.* **2016**, *15*, 1113−1119.

(11) Hamdi, H.; Salje, E. K. H.; Ghosez, P.; Bousquet, E. First-Principles Reinvestigation of Bulk WO_3. *Phys. Rev. B* **2016**, *94*, 245124.

(12) Mattoni, G.; Filippetti, A.; Manca, N.; Zubko, P.; Caviglia, A. D. Charge Doping and Large Lattice Expansion in Oxygen-Deficient Heteroepitaxial WO_3. *Phys. Rev. Mater.* **2018**, *2*, No. 053402.

(13) Leng, X.; Pereiro, J.; Strle, J.; Dubuis, G.; Bollinger, A. T.; Gozar, A.; Wu, J.; Litombe, N.; Panagopoulos, C.; Pavuna, D.; Božović, I. Insulator to Metal Transition in WO_3 Induced by Electrolyte Gating. *npj Quantum Mater.* **2017**, *2*, 35.

(14) Du, Y.; Gu, M.; Varga, T.; Wang, C.; Bowden, M. E.; Chambers, S. A. Strain Accommodation by Facile WO_6 Octahedral Distortion and Tilting during WO_3 Heteroepitaxy on $SrTiO_3(001)$. *ACS Appl. Mater. Interfaces* **2014**, *6*, 14253−14258.

(15) Svensson, J. S. E. M.; Granqvist, C. G. Modulated Transmittance and Reflectance in Crystalline Electrochromic WO_3 Films: Theoretical Limits. *Appl. Phys. Lett.* **1984**, *45*, 828−830.

(16) Svensson, J. S. E. M.; Granqvist, C. G. Electrochromic Coatings for Smart Windows: Crystalline and Amorphous WO_3 Films. *Thin Solid Films* **1985**, *126*, 31−36.

(17) Granqvist, C. G. Electrochromic Tungsten Oxide Films: Review of Progress 1993-1998. *Sol. Energy Mater. Sol. Cells* **2000**, *60*, 201−262.

(18) Mattoni, G.; de Jong, B.; Manca, N.; Tomellini, M.; Caviglia, A. D. Single-Crystal Pt-Decorated WO_3 Ultrathin Films: A Platform for Sub-ppm Hydrogen Sensing at Room Temperature. *ACS Appl. Nano Mater.* **2018**, *1*, 3446−3452.

(19) Crichton, W. A.; Bouvier, P.; Grzechnik, A. The First Bulk Synthesis of ReO_3-Type Tungsten Trioxide, WO_3, From Nanometric Precursors. *Mater. Res. Bull.* **2003**, *38*, 289−296.

(20) Dass, R. I.; Yan, J.-Q.; Goodenough, J. B. Oxygen Stoichiometry, Ferromagnetism, and Transport Properties of $La_{2-x}NiMnO_{6+\delta}$. *Phys. Rev. B* **2003**, *68*, 064415.

(21) Tilmans, H. A. C.; Elwenspoek, M.; Fluitman, J. H. J. Micro Resonant Force Gauges. *Sensors Actuators A Phys.* **1992**, *30*, 35−53.

(22) Kim, C. S.; Dickinson, S. M. The Flexural Vibration of Slightly Curved Slender Beams Subject to Axial End Displacement. *J. Sound Vib.* **1986**, *104*, 170−175.

(23) Bouwstra, S.; Geiselaers, B. On the Resonance Frequencies of Microbridges. In *TRANSDUCERS '91 1991 Int. Conf. Solid-State Sensors Actuators. Dig. Tech. Pap.*; IEEE: Piscataway, NJ, 1991; pp 538−542.

(24) Nayfeh, A. H.; Kreider, W.; Anderson, T. J. Investigation of Natural Frequencies and Mode Shapes of Buckled Beams. *AIAA J.* **1995**, *33*, 1121−1126.

(25) Lacarbonara, W.; Arafat, H. N.; Nayfeh, A. H. Non-Linear Interactions in Imperfect Beams at Veering. *Int. J. Non. Linear. Mech.* **2005**, *40*, 987−1003.

(26) Liu, X.; Fan, H.-Q. Electronic Structure, Elasticity, Debye Temperature and Anisotropy of Cubic WO_3 from First-Principles Calculation. *R. Soc. Open Sci.* **2018**, *5*, 171921.

DOI: 10.1021/acsami.9b14501
ACS Appl. Mater. Interfaces 2019, 11, 44438−44443